Research Article Vol. 11, No. 2 / 1 February 2021 / *Optical Materials Express* 219

Optical Materials EXPRESS

Epitaxial growth of ε-$(AlGa)_2O_3$ films on sapphire substrate by PLD and the fabrication of photodetectors

YANGYANG GAO,[1] QIAN FENG,[1,4] ZHAOQING FENG,[1] YAN ZUO,[1] YUNCONG CAI,[1] YACHAO ZHANG,[1] JING NING,[1] CHUNFU ZHANG,[1] XIAOJUAN SUN,[2] ZHITAI JIA,[3] JINCHENG ZHANG,[1,5] AND YUE HAO[1]

[1] *Wide Bandgap Semiconductor Technology Disciplines State Key Laboratory, Xidian University, Xi'an, 710071, China*
[2] *State Key Laboratory of Luminescence and Applications, Changchun Institute of Optics, Chinese Academy of Sciences, Changchun, 130033, China*
[3] *State Key Laboratory of Crystal Materials and Key Laboratory of Functional Crystal Materials and Device, Shandong University, Jinan, 250100, China*
[4] *qfeng@mail.xidian.edu.cn*
[5] *jchzhang@xidian.edu.cn*

Abstract: Pure phase ε-$(AlGa)_2O_3$ films were deposited utilizing pulsed laser deposition (PLD) on a sapphire (0001) substrate under the assistance of tin element. High resolution X-ray diffraction (HRXRD) reveals the presence of out-of-plane compressive strain in ε-$(AlGa)_2O_3$ films. From XPS and TEM measurements, an increase in oxygen pressure causes a reduction in Al content and a rise in the film growth rate. Moreover, the ε-$(AlGa)_2O_3$ films achieve a wider bandgap with a decrease in oxygen pressure, determined by the transmittance spectra and responsivity. For oxygen pressure increasing from 0.006mbar to 0.01mbar and 0.03mbar, the responsivity of the MSM photodetectors are 0.86A/W, 1.87A/W, and 4.38A/W, and an external quantum efficiency (EQE) of 448%, 946%, and 2114%, respectively, indicating larger gains in ε-$(AlGa)_2O_3$ devices.

1. Introduction

Recently, the growth of Ga_2O_3 film and the fabrication of Ga_2O_3 devices have received considerable attention owing to the Ga_2O_3 exceptional properties, such as large bandgap (E_g=4.55-5.03 eV), high theoretical breakdown electric field (E_{br}=8MV/cm) and physical and chemical stabilities [1]. ε-Ga_2O_3 is one of metastable forms of Ga_2O_3, a high symmetry hexagonal system with space group $P6_3mc$ [2–3]. Therefore, ε-Ga_2O_3 possesses a high polarization-induced two-dimensional electron gas with high sheet carrier densities up to $\sim10^{14}cm^{-2}$ in heterostructures with other materials [4]. With Al or In element incorporated into Ga_2O_3, the bandgap of ternary alloys can be tuned by changing the mole fractions. Al_2O_3 is very suitable to alloy with ε-Ga_2O_3 because Al_2O_3 has an extraordinarily large bandgap (8.8 eV) [5] and the electron configuration of Al atom is similar to that of Ga atom. Till now, the pure phase ε-Ga_2O_3 film has been achieved by halide vapor phase epitaxy (HVPE) [6], metal organic chemical vapor deposition (MOCVD) [7–10], pulsed laser deposition (PLD) [11–12], mist chemical vapor deposition [13–14] and molecular beam epitaxy (MBE) [15]. Furthermore, the single phase ε-$(AlGa)_2O_3$ and ε-$(InGa)_2O_3$ films have been grown on AlN and sapphire substrates, respectively [16–19].

Solar-blind deep-UV (DUV) photodetectors have various applications in monitoring ozone holes, detecting flame, space communication, and inspection of UV leakage [20–24]. ε-Ga_2O_3 is a promising candidate for deep-UV or solar-blind photodetector applications owing to the large absorption coefficient of about 10^5 cm^{-1} for the wavelength shorter than 260 nm. Bandgap

#413500
Journal © 2021

https://doi.org/10.1364/OME.413500
Received 26 Oct 2020; revised 6 Dec 2020; accepted 14 Dec 2020; published 4 Jan 2021

engineering of ε-$(AlGa)_2O_3$ or ε-$(InGa)_2O_3$ ternary alloying films enables detection wavelength of the ultraviolet photodetectors to be modulated in the deep ultraviolet band [25]. However, there have been few reports on the fabrication and characterization of ε-$(AlGa)_2O_3$ or ε-$(InGa)_2O_3$ devices.

Herein, the single crystal ε-$(AlGa)_2O_3$ film was deposited on sapphire substrate by pulsed laser deposition (PLD) under the assistance of tin element and the influence of oxygen pressure on the film properties was studied. In addition, the metal-semiconductor-metal (MSM) photodetectors were fabricated on ε-$(AlGa)_2O_3$ epilayers and the electrical characteristics were also investigated.

2. Experimental details

The ε-$(AlGa)_2O_3$ films were grown by PLD under the assistance of Sn on double-polished (0001)-oriented sapphire substrates with ε-Ga_2O_3 as the buffer layer. Using a KrF excimer laser ($\lambda = 248$ nm, 20 ns pulse duration), the $(AlGa)_2O_3$ ceramic target with Al atom percent of 6% and Sn atom percent of 1% was used for the film growth and the Ga_2O_3 ceramic target with Sn atom percent of 1% for the buffer layer deposition. The base pressure in the chamber was 7×10^{-8} mbar. During growth, the temperature was fixed at 570°C, the laser energy density was 2.0 J/cm^2 and the repetition rate was 3 Hz for a total deposition of 8000 pulses, 2000 pulses for ε-Ga_2O_3 buffer layer and 6000 pulses for ε-$(AlGa)_2O_3$ film, respectively. The oxygen partial pressure was kept at 0.01mbar during ε-Ga_2O_3 buffer layer deposition while the ε-$(AlGa)_2O_3$ epilayers were deposited at different oxygen pressure of 0.006 mbar (Sample A), 0.01 mbar (Sample B) and 0.03 mbar (Sample C), respectively. Growth conditions for the samples used in this work are listed in Table 1. The crystal structures of ε-$(AlGa)_2O_3$ films were investigated by x-ray diffraction (XRD) measurement utilizing theta-2theta (θ-2θ) scans with Cu Kα radiation ($\lambda = 0.15406$ nm), while the scan range between 10° and 70° and scan speed is 8 (deg/min). The transmission electron microscopy (TEM) was done with HT7700 equipment, x-ray photoelectron spectroscopy (XPS) measurements were performed using a Kratos Analytical Axis Ultra XPS equipped with monochromatic Al Kα ($hv = 1486.6$ eV) x-ray radiation source, the optical transmittance was measured with a Lambda 900 double-beam UV-vis-NIR spectrophotometer. The metal-semiconductor-metal (MSM) photodetectors were fabricated with standard photolithography and lift-off techniques. Figure 1 shows cross-sectional device with MSM structure. The total length of interdigital Ti/Au (10 nm/100 nm) metal electrodes is 1.75 mm and finger spacing is 100 µm. The current-voltage (I-V) and time-dependent photo-response measurements of the MSM photodetectors were carried out using an Agilent B1500A Semiconductor Device Analyzer. The responsivity R was measured with a SPEX scanning monochromator employing a Xe lamp as the illumination source.

Table 1. The growth conditions with sample A, B and C

Samples	Pulse number for Ga_2O_3 buffer	$P(O_2)$ for Ga_2O_3 Growth (mbar)	Ga_2O_3 buffer Thickness (nm)	Pulse number for $(AlGa)_2O_3$	$P(O_2)$ for $(AlGa)_2O_3$ Growth (mbar)	$(AlGa)_2O_3$ buffer Thickness (nm)	Pulse energy density (J/cm^2)
Sample A	2000	0.01	98	6000	0.006	158	2.0
Sample B	2000	0.01	97	6000	0.01	167	2.0
Sample C	2000	0.01	98	6000	0.03	196	2.0

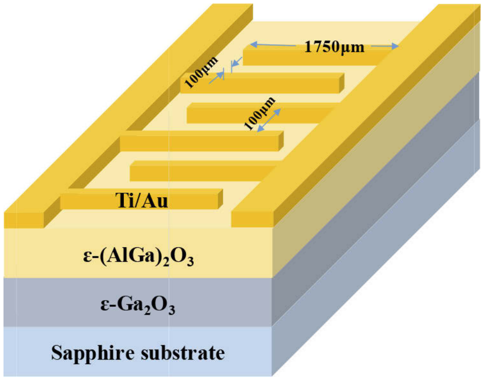

Fig. 1. The crossing sectional schematic diagram of the fabricated ε-(AlGa)$_2$O$_3$ solar-blind photodetector with MSM structure.

3. Results and discussion

3.1. *Material characterization*

As shown in Fig. 2(a), the peak at 41.68° is the diffraction of the sapphire (0006) planes, the peak at 19.20° is indexed as ε-Ga_2O_3 (0002) and those around at 39° and 60° can be fitted by two Gaussian curves with peaks at 38.90° and 39.02°, 59.86° and 60.12°(Sample A), the former are attributed to the diffraction of the ε-Ga_2O_3 and ε-$(AlGa)_2O_3$ (0004) planes while the latter to the (0006) planes, respectively. Figure 1(b) and (c) show the magnified image of the (0004) planes and (0006) planes resolved into two separate peaks corresponding to ε-Ga_2O_3 and ε-$(AlGa)_2O_3$. Considering all the fitting procedures, experimental errors etc., the error estimation of degree and plane spacing with the ε-Ga_2O_3 and ε-$(AlGa)_2O_3$ (0002), (0004) and (0006) planes are presented in Fig. 2(d) and (e). It was observed that degree and plane spacing values are consistent and repeatable with very slight and negligible changes over all the films. The diffraction peak at 19.19° cannot be resolved into two separate peaks, owing to the diffraction peaks of ε-Ga_2O_3 and ε-$(AlGa)_2O_3$ (0002) planes are too close to be distinguished. The diffraction angles of ε-Ga$_2$O$_3$ are larger than those of powder ε-Ga_2O_3 (PDF#06-0509), which may be due to an in-plane tensile strain and out-of-plane compressive strain in the ε-Ga_2O_3 buffer layers [11]. Furthermore, we can clearly observe that ε-$(AlGa)_2O_3$ peaks are right next to those of ε-Ga_2O_3, indicating that ε-$(AlGa)_2O_3$ epilayer has smaller interface distance than ε-Ga_2O_3. With oxygen partial pressure increasing (Sample A-C), the diffraction peaks of ε-$(AlGa)_2O_3$ shift to the lower angle side, such as 39.02°, 39.00° and 38.96° for (0004) planes while 60.12°, 60.08° and 60.03° for the (0006) planes of Sample A, B and C, respectively. According to Bragg's law, the spacings of ε-$(AlGa)_2O_3$ (0004) and (0006) planes are 0.2306 nm, 0.2308 nm, 0.2310 nm and 0.1538 nm, 0.1539 nm, 0.1540 nm for Sample A-C, respectively, which are 0.36%, 0.32%, 0.30% and 0.32%, 0.30%, 0.29% smaller than that calculated based on the data in [16,18], indicating that ε-$(AlGa)_2O_3$ suffers out-of-plane compressive strain for a smaller ionic radius of Al than that of Ga and with oxygen pressure increasing, the compressive strain gradually decreasing. Furthermore, the full-width at half-maximum (FWHM) value of the (0006) diffraction peak of ε-(AlGa)$_2$O$_3$ were 0.143°, 0.118° and 0.114° for three simples respectively, implying that the crystal quality of ε-(AlGa)$_2$O$_3$ were improved with oxygen pressure increasing.

Figure 3 depicts the TEM image of ε-$(AlGa)_2O_3$ film (Sample B). It is obvious that ε-$(AlGa)_2O_3$ and ε-Ga_2O_3 films present columnar contrasts, demonstrating a columnar growth of the material. Figure 3(b) presents a magnified view of the interface between ε-$(AlGa)_2O_3$ and ε-Ga_2O_3, indicating that single crystal ε-$(AlGa)_2O_3$ is grown on ε-Ga_2O_3 buffer layer and

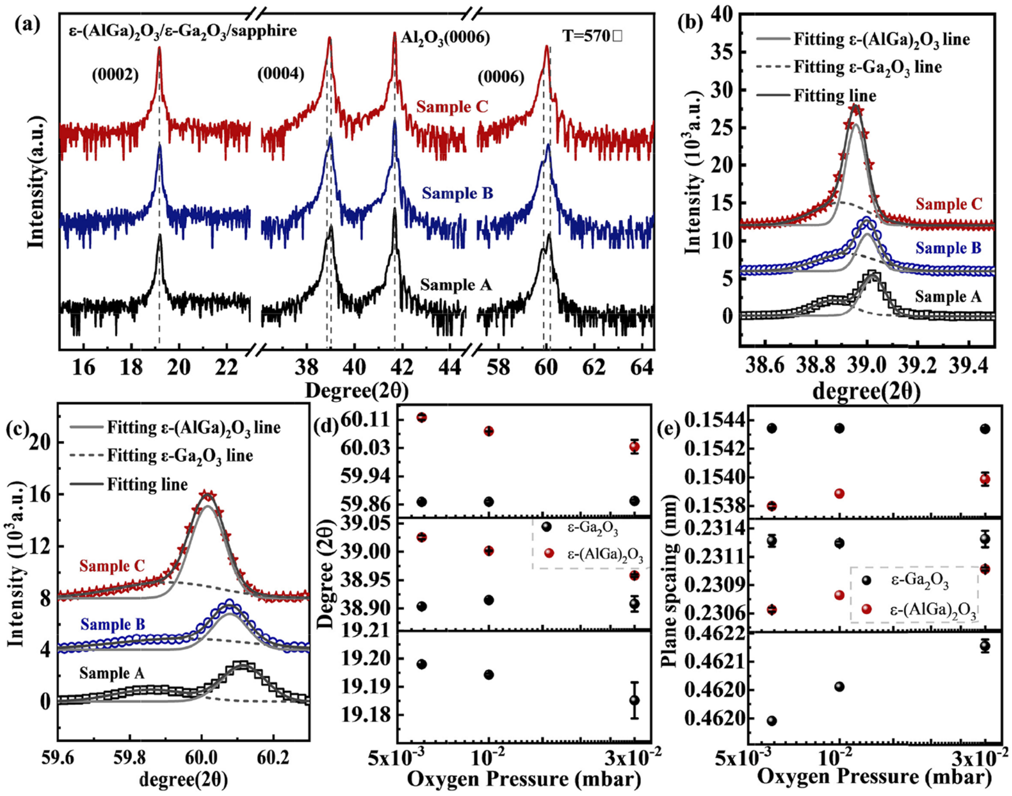

Fig. 2. (a) HRXRD diffraction curves (logarithmic scales) of ε-$(AlGa)_2O_3$/ε-Ga_2O_3 samples deposited on sapphire (0001) substrate under the assistance of Sn element. Magnified image of (b) (0004) and (c) (0006) diffraction peak can be resolved into two separate peaks corresponding to ε-Ga_2O_3 and ε-$(AlGa)_2O_3$. The XRD degree (d) and (e) plane spacing of the ε-Ga_2O_3 and ε-$(AlGa)_2O_3$ planes with various growth pressures.

there is no serious generation of dislocations at the interface. As described in reference [9,11], a polycrystalline Ga_2O_3 transition layer can be discerned at the ε-Ga_2O_3/sapphire substrate interface. The thickness of the ε-Ga_2O_3 buffer layer is about 98 nm while those of the ε-$(AlGa)_2O_3$ films are 158 nm, 167 nm and 190 nm for three samples respectively. With higher oxygen partial pressure, the higher growth rate can be realized for suppressing $(AlGa)_2O_3$ decomposition into suboxide and the following desorption from substrate surface. Therefore, the higher the oxygen pressure, the less the suboxide formation and the higher the growth rate.

The chemical states of the elements in ε-$(AlGa)_2O_3$ epilayers were characterized by XPS. Before XPS measurement, several atomic layers of the film surface were etched by in situ Ar^+ plasma. All spectra were calibrated with standard C1s peak (284.6 eV). The Al2p, Ga2p3/2 and O1s spectra are presented in Fig. 4. Gaussian-Lorentzian mixed function is used to simulate the experimental spectra by the fitting program Thermo Avantage. Based on the peak area and taken the sensitivity factor into account, the Al to Ga atom ratios in ε-$(AlGa)_2O_3$ films are 5.4:94.6, 4.5:95.5 and 0.8:99.2 for Sample A, Sample B and Sample C, respectively. For low oxygen pressure, aluminum atoms are more likely to be incorporated than Ga atoms due to higher dissociation energy of the Al-O bond compared to the Ga-O bond. In addition, gallium forms volatile sub-oxides being desorbed [18,26]. With oxygen pressure increasing, more gallium gets incorporated into the thin film and the Al percentage was reduced which is consistent with AFM

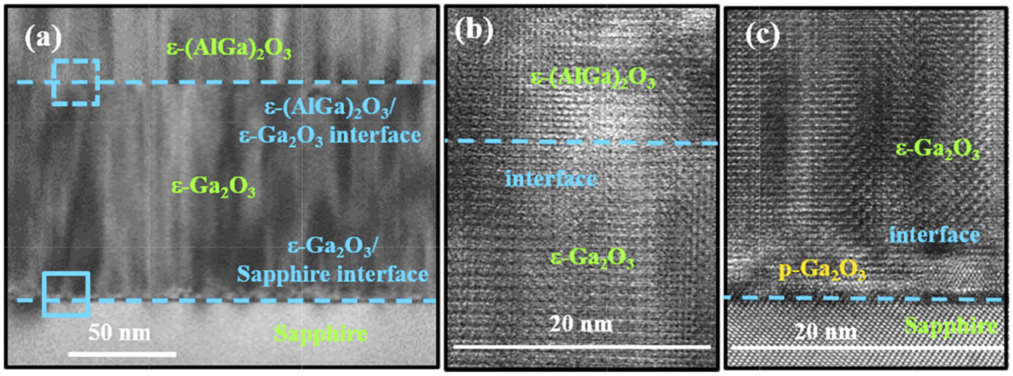

Fig. 3. TEM images of (a) an overview of Sample B, (b) and (c) High resolution TEM images of the selected regions in blue dashed and blue solid boxes in (a), respectively, showing the single crystallinity of ε-$(AlGa)_2O_3$ and ε-Ga_2O_3 layers.

results. The Al2p spectra of ε-$(AlGa)_2O_3$ films are shown in Fig. 4(a). As oxygen pressure is increasing, the Al2p peak intensity becomes weaker and the peak shifts towards lower binding energy, illustrating less Al percentage in the epilayer to form Al-O-Ga bonds. The shift can be ascribed to the fact that Ga has a more ionic character than Al in ε-$(AlGa)_2O_3$ films [27]. Furthermore, the Ga2p3/2 can be decomposed into two Gaussian peaks, the Ga-O bond of $(AlGa)_2O_3$ and that of $(AlGa)_2O_x(x<3)$ suboxide, respectively. The FWHM of the fitted peak positions and atomic ratio for Ga2p3/2 spectra obtained from Fig. 4(b) are summarized in Table 2. From Fig. 4(b), we can calculate the ratios between $(AlGa)_2O_x(x<3)$ suboxide and $(AlGa)_2O_3$ are 0.11, 0.08 and 0.06 for Sample A, B and C, respectively. Therefore, higher oxygen pressure can restrain the formation of $(AlGa)_2O_x$ suboxide and promote the growth of $(AlGa)_2O_3$. Moreover, the binding energy peak of O1s at 531.08 eV for ε-$(AlGa)_2O_3$ is similar to that of ε-Ga_2O_3[11]. Specially, the oxygen percent in ε-$(AlGa)_2O_3$ samples was between 42.3% and 46.6%, indicating that there are lots of oxygen vacancies in the ε-$(AlGa)_2O_3$ films. Figure 4(d) depicts XPS fitting results for spectra of sample A. The Sn3d peak is fitted as three sub peaks assigned to $Sn^{4+}3d_{5/2}$ (~488.1 eV), Sn^0(~491.1 eV) and $Sn^{4+}3d_{3/2}$ (~495.8 eV), respectively [28]. The Sn^{4+} to Sn^0 atom ratio in sample A is 97.5:2.5, indicating majority of Sn atoms exhibit the tetravalent Sn^{4+} oxidation state in ε-$(AlGa)_2O_3$ films. Sn atoms occupy the octahedral lattice site and promote the formation of ε-phase with more octahedral lattice site, like the catalyst [11–12].

Table 2. The Ga atomic percentages and bonding analysis of sample A, B and C

$(AlGa)_2O_x$	B.E.	FWHM	Area	Ratio%
Sample A	1115.3	2.71	56281.63	10.27
Sample B	1115.4	2.51	60627.16	7.57
Sample C	1115.7	2.18	31031.19	6.07

$(AlGa)_2O_3$	B.E.	FWHM	Area	Ratio%
Sample A	1117.3	2.49	489086.58	89.73
Sample B	1117.4	1.93	500095.63	92.43
Sample C	1117.4	1.96	478938.82	93.93

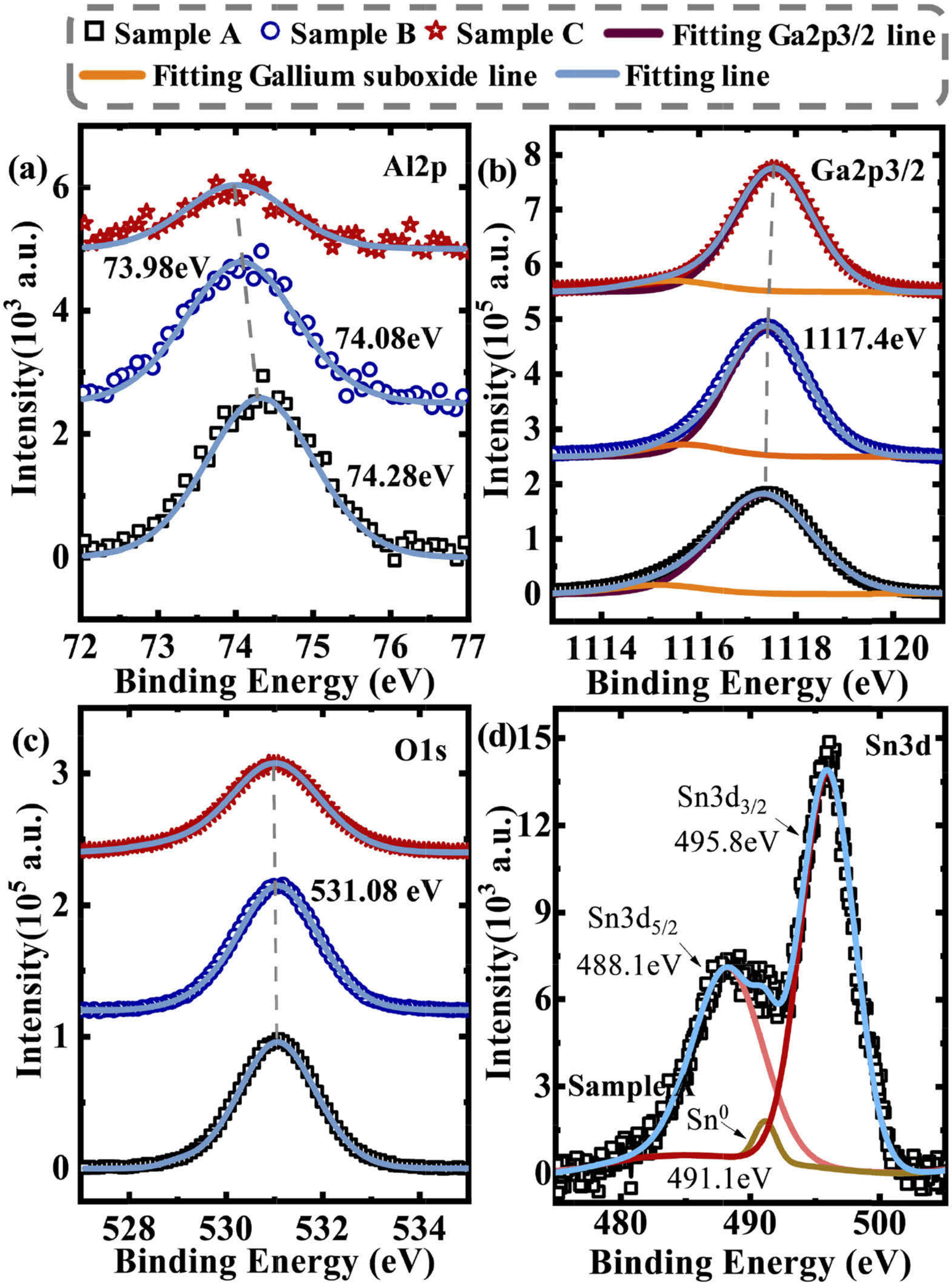

Fig. 4. XPS spectra of (a) Al2p, (b) Ga2p3/2, and (c) O1s spectra of ε-(AlGa)$_2$O$_3$ samples (d) Sn3d of sample A. Gray dash line are guides to the eyes.

Figure 5 shows the surface morphology of ε-(AlGa)$_2$O$_3$ epilayers using atomic force microscopy (AFM) with scanning area of 5μm×5μm and the pixel size of 256×256. The root-mean-square (RMS) roughness of Sample A, Sample B and Sample C are 0.919 nm, 0.820 nm and 0.594 nm, respectively, that is, with oxygen partial pressure increasing, the surface roughness decreasing may result from the increase of the films thickness [12].

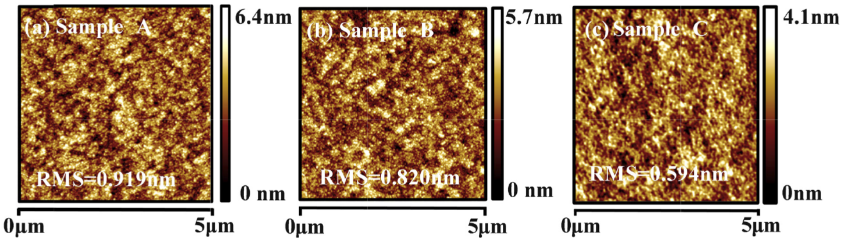

Fig. 5. AFM images of ε-(AlGa)$_2$O$_3$ films grown at different oxygen partial pressure (a) Sample A, (b) Sample B, (c) Sample C.

Figure 6 depicts the transmittance spectra of ε-(AlGa)$_2$O$_3$ films. As can be seen from Fig. 6(a), there is a sharp absorption edge located at around 250 nm and with Al composition increasing, the absorption edge of ε-(AlGa)$_2$O$_3$ shifts towards shorter wavelength. It is obvious that the average transmittance is over 70% as the wavelength longer than 300 nm. The absorption coefficient α can be calculated by the equation $\alpha = (1/t)\ln[(1 - R_C)^2/T]$ and the plots of $(\alpha h\nu)^2$ vs $h\nu$ also can be obtained on the basis of $\alpha h\nu = (h\nu - E_g)^2$ [29], where α, t, h, ν, R_c and T are absorption coefficient, film thickness, Planck constant, frequency, the reflectance and transmittance, respectively. The thicknesses of the epilayers were determined by HRTEM. The optical bandgap can be extracted by extrapolating the linear region of the plots $(\alpha h\nu)^2$ vs $h\nu$ to the horizontal axis, as shown in Fig. 6(b), about 5.27 eV, 5.20 eV and 5.07 eV for Sample A, B and C, respectively.

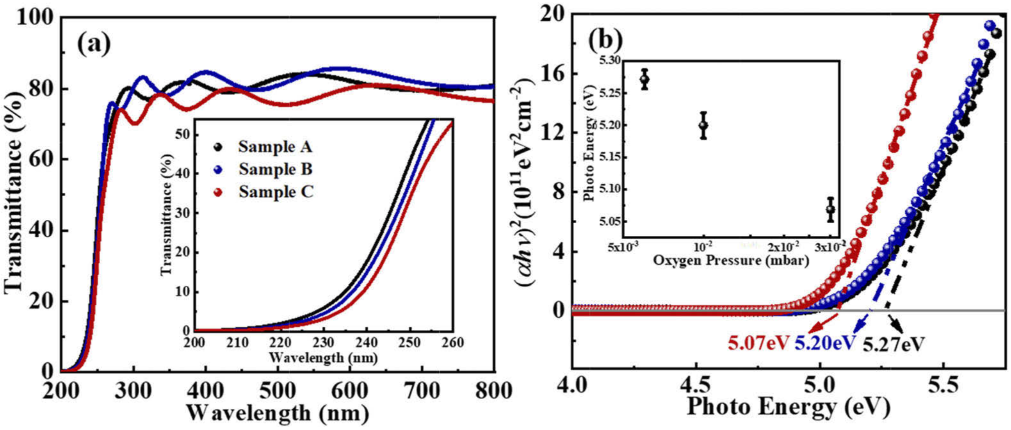

Fig. 6. (a) Transmittance spectra of ε-(AlGa)$_2$O$_3$ films (Sample A-C) deposited on sapphire substrate with ε-Ga$_2$O$_3$ as buffer layer. Inset: Magnified view of transmittance spectra of ε-(AlGa)$_2$O$_3$. (b) $(\alpha h\nu)^2$ vs $h\nu$ curves and linear extrapolation for estimating the optical bandgap, Inset: Bandgap variation of ε-(AlGa)$_2$O$_3$ thin films deposited at with various growth pressures.

3.2. Photoelectric characteristics of the devices

To investigate the photoelectric characteristics of the ε-(AlGa)$_2$O$_3$ UV photodetectors, we carried out the current-voltage (I-V) measurements under dark (I_{dark}) and illuminated by 254 nm light with various light intensities (I_{photo}), such as 50, 100 and 200 µW/cm^2, as presented in Fig. 7. The photocurrents increase almost linearly with bias voltage (V_{bias}) and illumination power density for three samples. The linear I-V curve showed ohmic contact characteristics with the Ti/Au electrodes, may be ascribed to the oxygen vacancies in the ε-(AlGa)$_2$O$_3$ film near the Ti/Au and ε-(AlGa)$_2$O$_3$ interface [30]. The Fermi level of ε-(AlGa)$_2$O$_3$ can be pinned close to the defect levels of oxygen vacancies, which causes the depletion region between Ti/Au and ε-(AlGa)$_2$O$_3$ to become narrower. The narrow depletion region allows the electrons to tunnel through the barrier, thus leading to an Ohmic electron transport [31]. It is found that the dark current gradually decreases with the increases in oxygen pressure from 0.006mbar to 0.01mbar and 0.03mbar. Owing to the reduction of oxygen vacancies which provide a mechanism for charge hopping, the sample grown at higher oxygen pressure becomes more resistive, hence leading to the lower dark current [32–33]. The photocurrent increases from 1.16×10^{-8} A to 2.36×10^{-8} A as the oxygen pressure increases from 0.006mbar to 0.03mbar at V_{bias}=20 V and P_{light} = 200 µW/cm^2. With higher oxygen pressure, superior crystalline quality of the ε-(AlGa)$_2$O$_3$ film results in the photocurrent increment of the ε-(AlGa)$_2$O$_3$ photodetector. The photo to dark current ratio (PDCR) of Sample C is about 305, higher than other two devices, calculated by $(I_{photo} - I_{dark})/I_{dark}$ expression.

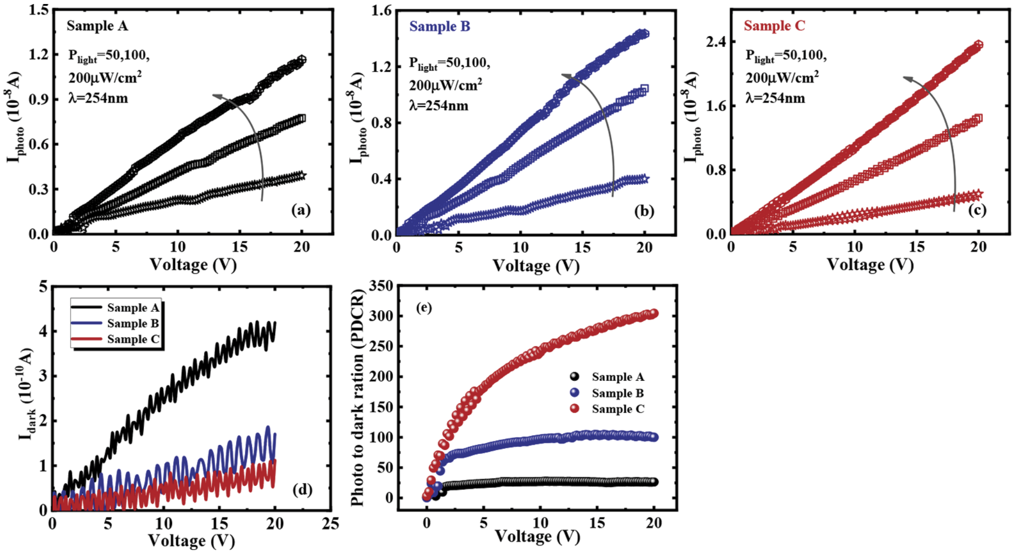

Fig. 7. Characteristics of I_{photo} versus voltage(a)(b)(c) and (d) I_{dark} versus voltage (e) PDCR for the ε-(AlGa)$_2$O$_3$ photodetectors of Sample A-C.

Figure 8 depicts the time-dependent photoresponse characteristics of the photodetectors. During measurements, an illumination λ of 254 nm square-wave light was used with V_{bias} of 20 V, P_{light} of 200 μW/cm^2 and period of 60s. After several periods, the photodetectors still exhibit almost the same photoresponse characteristics, indicating the device of high stability and excellent repeatability. Under UV illumination, the photocurrents rise to around 16 nA, 18 nA and 24 nA for Sample A, Sample B and Sample C, respectively. When the UV light is turned off, the currents decrease rapidly. The rise and decay processes usually can be divided into a fast response and a slow response [34], the fast response associated with the band to band transition while the slow-response related to the recombination of photo-generated carriers captured by the defect levels. For the quantitative analysis, the rise and decay processes were both fitted by bi-exponential relaxation curves, based on the following equation [35–36]:

$$I = I_0 + A\mathrm{e}^{-t/\tau_1} + B\mathrm{e}^{-t/\tau_2}$$

where I_0 is steady state photocurrent, A and B are constants, t, τ_1 and τ_2, are time and time constants, respectively. Figure 8(b-d) depicts the fitting curves and two time constants during rise and decay processes for Sample A-C. With oxygen pressure increasing, the decay time constants τ_{d2} decreases from 4.84s to 4.09s and 2.75s, demonstrating much more defects in Sample A than the other two samples, thus causing more significant persistent photoconductivity (PPC).

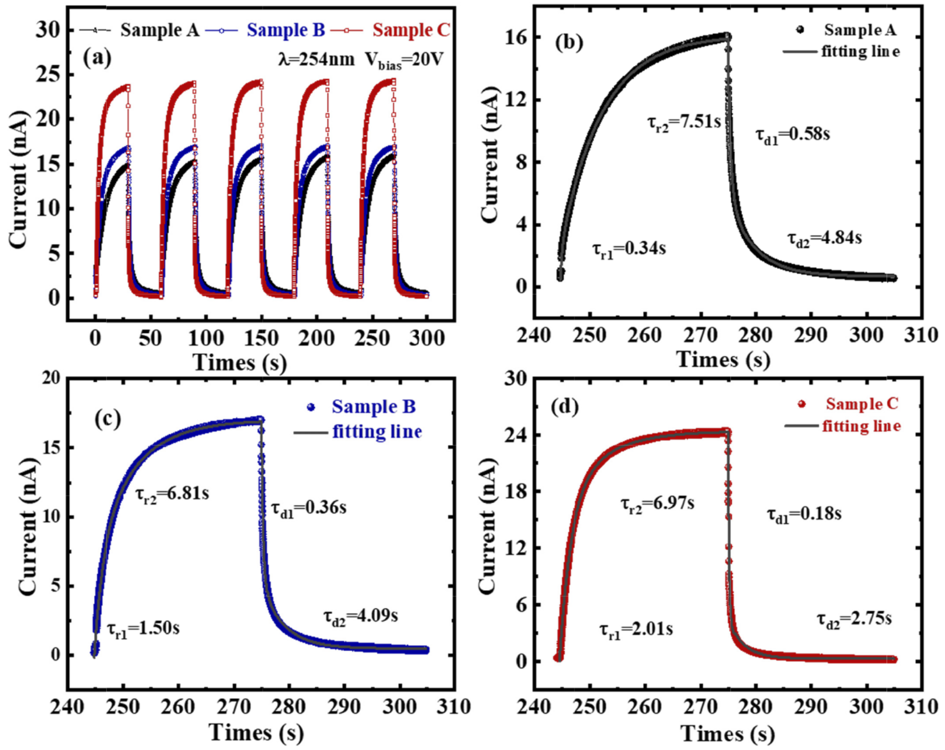

Fig. 8. (a) Time-dependent I_{photo} characteristics for ε-(AlGa)$_2$O$_3$ photodetectors under a V_{bias} of 20 V (b-d) the current response and recovery bi-exponential fitting of Sample A-C.

Figure 9 shows the variation of responsivity R with the illumination wavelengths λ for the ε-(AlGa)$_2$O$_3$ photodetectors. The maximum responsivity (R_{max}) at the bias voltage of 40 V are 0.86A/W, 1.87A/W and 4.38A/W for Sample A-C, respectively, that is, Sample C achieves the highest responsivity among the three samples. As the cutoff wavelength is defined as where the responsivity equals $\sqrt{1/2}R_{max}$, the bandgaps were determined to be 5.28 eV (235 nm), 5.18 eV (239 nm), and 5.08 eV (244 nm), which is in consistent with the transmittance results. The external quantum efficiency (EQE) for the ε-(AlGa)$_2$O$_3$ photodetectors is calculated by

$$EQE = \frac{hcR_{\max}}{e\lambda} = \frac{hc(I_{photo} - I_{dark})}{e\lambda PS} \tag{6}$$

where R_{max} is the responsivity of a photodetector, h is Planck's constant, c is the velocity of light, e is the basic electron charge, and λ is the incident light wavelength, I_{photo} is the dark current,

I_{dark} is the dark current, P is the power density of incident light, and S is the effective illuminated area [37]. The external quantum efficiency (EQE) of three photodetectors were 448%, 946%, and 2114%, respectively. The EQE of the ε-$(AlGa)_2O_3$ photodetector with an oxygen pressure of 0.03mbar can reach 2114%, which is ~3.91 times greater than that of the ε-Ga_2O_3 photodetector and ~2.71 times than that of β-$(Al_{0.12}Ga_{0.88})_2O_3$ photodetector, indicating there is larger gains in ε-$(AlGa)_2O_3$ device than in β-$(Al_{0.12}Ga_{0.88})_2O_3$ [11,38].

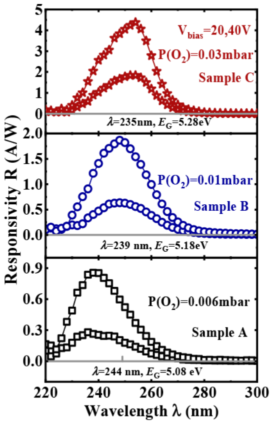

Fig. 9. The dependence of R versus illumination wavelengths λ for the different photodetectors at $V_{bias} = 20$ and 40 V.

The decay time of ε-$(AlGa)_2O_3$ photodetectors decreased with the oxygen pressure increasing. On the one hand, with higher oxygen pressure, the reduction of decay time might originate from superior crystalline quality of the ε-$(AlGa)_2O_3$ film. On the other hand, with higher oxygen pressure, a reduction decay time of ε-$(AlGa)_2O_3$ photodetectors indicates that ε-$(AlGa)_2O_3$ thin films have less surface and bulk traps preventing carriers' recombination [31]. Fewer photogenerated carriers are trapped and the effective lifetime of those carriers in the ε-$(AlGa)_2O_3$ photodetectors gets longer under increasing oxygen pressure. Moreover, the photoconductive gain can be expressed as $G = \tau/t$, where τ is the carrier recombination time and t is the carrier transit time. It is obvious that photoconductive gain is positively correlated with the carrier lifetime [39]. Therefore, the higher photoconductive gain of ε-$(AlGa)_2O_3$ photodetectors can be obtained under higher oxygen pressure.

4. Conclusion

The single crystal ε-$(AlGa)_2O_3$ films with ε-Ga_2O_3 as buffer layer were deposited on sapphire (0001) substrates using PLD under the assistance of Sn element. The HRXRD reveals that ε-$(AlGa)_2O_3$ interplane spacing is smaller than the theoretical values. The XPS and TEM illustrate that the Al composition decreases and thickness of ε-$(AlGa)_2O_3$ increases with oxygen pressure increasing. As Al content increasing, the photocurrent apparently decreases, which may be ascribed to defects trap much more photo-generated carriers. The EQE of the ε-$(AlGa)_2O_3$ photodetector with an oxygen pressure of 0.03mbar can reach 2114%, which is ~3.91 times greater than that of the ε-Ga_2O_3 photodetector and ~2.71 times than that of β-$(Al_{0.12}Ga_{0.88})_2O_3$ device.

Funding. National Key Research and Development Program of China (Grant No. 2018YFB0406500); National Natural Science Foundation of China (61774116, 61974112, 61974115, 51932004); State Key Laboratory of Luminescence and Applications (Grant No. SKLA-2020-04); Key Technology Research and Development Program of Shandong (2018CXGC0410); the 111 Project 2.0 (Grant No: BP2018013).

Disclosures. The authors declare that they have no known competing financial interests or personal relationships that could have appeared to influence the work reported in this paper.

References

1. M. Higashiwaki, K. Sasaki, A. Kuramata, T. Masui, and S. Yamakoshi, "Development of gallium oxide power devices," Phys. Status Solidi A **211**(1), 21–26 (2014).
2. H. Y. Playford, A. C. Hannon, E. R. Barney, and R. I. Walton, "Structures of uncharacterized polymorphs of gallium oxide from total neutron diffraction," Chem. Eur. J. **19**(8), 2803–2813 (2013).
3. K. Matsuzaki, H. Yanagi, T. Kamiya, H. Hiramatsu, K. Nomura, M. Hirano, and H. Hosono, "Field-induced current modulation in epitaxial film of deep-ultraviolet transparent oxide semiconductor Ga2O3," Appl. Phys. Lett. **88**(9), 092106 (2006).
4. M. B. Maccioni and V. Fiorentini, "Phase diagram and polarization of stable phases of $(Ga_{1-x}Inx)_2O_3$," Appl. Phys. Express **9**(4), 041102 (2016).
5. D. Liu, S. J. Clark, and J. Robertson, "Oxygen vacancy levels and electron transport in Al_2O_3," Appl. Phys. Lett. **96**(3), 032905 (2010).
6. Y. Oshima, E. G. Villora, Y. Matsushita, S. Yamamoto, and K. Shimamura, "Epitaxial growth of phase-pure ε-Ga_2O_3 by halide vapor phase epitaxy," J. Appl. Phys. **118**(8), 085301 (2015).
7. F. Boschi, M. Bosi, T. Berzina, E. Buffagni, C. Ferrari, and R. Fornari, "Hetero-epitaxy of ε-Ga_2O_3 layers by MOCVD and ALD," J. Cryst. Growth **443**, 25–30 (2016).
8. F. Mezzadri, G. Calestani, F. Boschi, D. Delmonte, M. Bosi, and R. Fornari, "Crystal structure and Ferroelectric properties of ε-Ga_2O_3 films grown on (0001)-sapphire," Inorg. Chem. **55**(22), 12079–12084 (2016).
9. Y. Chen, X. Xia, H. Liang, Q. Abbas, Y. Liu, and G. Du, "Growth pressure controlled nucleation epitaxy of pure phase ε-and β-Ga_2O_3 films on Al_2O_3 via MOCVD," Cryst. Growth Des. **18**(2), 1147–1154 (2018).
10. X. Xia, Y. Chen, Q. Feng, H. Liang, P. Tao, M. Xu, and G. Du, "Hexagonal phase-pure wide band gap ε-Ga_2O_3 films grown on 6H-SiC substrates by metal organic chemical vapor deposition," Appl. Phys. Lett. **108**(20), 202103 (2016).
11. Y. Cai, K. Zhang, Q. Feng, Y. Zuo, Z. Hu, Z. Feng, H. Zhou, X. Lu, Ch. Zhang, W. Tang, J. Zhang, and Y. Hao, "Tin-assisted growth of ε-Ga2O3 film and the fabrication of photodetectors on sapphire substrate by PLD," Opt. Mater. Express **8**(11), 3506–3517 (2018).
12. M. Kneiß, A. Hassa, D. Splith, C. Sturm, H. Wenckstern, T. Schultz, N. Koch, M. Lorenz, and M. Grundmann, "Tin-assisted heteroepitaxial PLD-growth of κ-Ga_2O_3 thin films with high crystalline quality," APL Mater. **7**(2), 022516 (2019).
13. D. Tahara, H. Nishinaka, S. Morimoto, and M. Yoshimoto, "Stoichiometric control for heteroepitaxial growth of smooth ε-Ga_2O_3 thin films on c-plane AlN templates by mist chemical vapor deposition," Jpn. J. Appl. Phys. **56**(7), 078004 (2017).
14. H. Nishinaka, D. Tahara, and M. Yoshimoto, "Heteroepitaxial growth of ε-Ga_2O_3 thin films on cubic (111) MgO and (111) yttria-stablized zirconia substrates by mist chemical vapor deposition," Jpn. J. Appl. Phys. **55**(12), 1202BC (2016).
15. M. Kracht, A. Karg, J. Schormann, M. Weinhold, D. Zink, F. Michel, M. Rohnk, M. Schowalter, B. Gerken, A. Rosenauer, P. J. Klar, J. Janek, and M. Eickhoff, "Tin-assisted synthesis of ε-Ga_2O_3 by molecular beam epitaxy," Phys. Rev. Appl. **8**(5), 054002 (2017).
16. D. Tahara, H. Nishinaka, S. Morimoto, and M. Yoshimoto, "Heteroepitaxial growth of ε-$(Al_xGa_{1-x})_2O_3$ alloy films on c-plane AlN templates by mist chemical vapor deposition," Appl. Phys. Lett. **112**(15), 152102 (2018).
17. H. Nishinaka, N. Miyauchi, D. Tahara, S. Morimoto, and M. Yoshimoto, "Incorporation of indium into ε-gallium oxide epitaxial thin films grown via mist chemical vapour deposition for bandgap engineering," Crystengcomm **10**(13), 1039 (2018).
18. P. Storm, M. Kneiß, A. Hassa, T. Schultz, D. Splith, H. von Wenckstern, N. Koch, M. Lorenz, and M. Grundmann, "Epitaxial κ-$(Al_xGa_{1-x})_2O_3$ thin films and heterostructures grown by tin-assisted VCCS-PLD," APL Mater. **7**(11), 111110 (2019).
19. M. Kneiß, A. Hassa, D. Splith, C. Sturm, H. von Wenckstern, M. Lorenz, and M. Grundmann, "Epitaxial stabilization of single phase κ-$(In_xGa_{1-x})_2O_3$ thin films up to x = 0.28 on c-sapphire and κ-Ga_2O_3 (001) templates by tin-assisted VCCS-PLD," APL Mater. **7**(10), 101102 (2019).
20. H. Chen, K. Liu, L. Hu, A. A. Al-Ghamdi, and X. Fang, "New concept ultraviolet photodetectors," Mater. Today **18**(9), 493–502 (2015).
21. C. O. Kim, S. Kim, D. H. Shin, S. S. Kang, J. M. Kim, C. W. Jang, S. S. Joo, J. S. Lee, J. H. Kim, S.-H. Choi, and E. Hwang, "High photo responsivity in an all-graphene p–n vertical junction photodetector," Nature Communication **5**(1), 1–7 (2014).
22. F. Alema, B. Hertog, A. V. Osinsky, P. Mukhopadhyay, M. Toporkov, W. V. Schoenfeld, E. Ahmadi, and J. Speck, "Vertical solar blind Schottky photodiode based on homoepitaxial Ga2O3 thin film," Proc. SPIE **10105**, 101051M (2017).
23. Y. Qin, H. Dong, S. B. Long, Q. M. He, G. Z. Jian, Y. Zhang, X. Z. Zhou, T. Y u, X. H. Hou, T. J. Tan, Z. F. Zhang, Q. Liu, H. B. Lv, and M. Liu, "Enhancement-mode β-Ga_2O_3 metal–oxide–semiconductor field-effect solar-blind phototransistor with ultrahigh detectivity and photo-to-dark current ratio," IEEE Electron Device Lett. **40**(5), 742–745 (2019).

24. L. Sang, M. Liao, and M. Sumiya, "A comprehensive review of semiconductor ultraviolet photodetectors: From thin film to one-dimensional nanostructures," Sensors **13**(8), 10482–10518 (2013).
25. M. Bosi, P. Mazzolini, L. Seravalli, and R. Fornari, "Ga_2O_3 polymorphs: tailoring the epitaxial growth conditions," J. Mater. Chem. C **8**(32), 10975–10992 (2020).
26. A. Hassa, H. von Wenckstern, L. Vines, and M. Grundmann, "Influence of oxygen pressure on growth of Si-doped β-$(Al_xGa1-x)_2O_3$ thin films on c-sapphire substrates by pulsed laser deposition," ECS J. Solid State Sci. Technol. **8**(7), Q3217–Q3220 (2019).
27. F. Zhang, K. Saito, T. Tanaka, M. Nishio, M. Arita, and Q. Guo, "Wide bandgap engineering of $(AlGa)_2O_3$ films Appl," Phys. Lett. **105**(16), 162107 (2014).
28. L. Yan, J. S. Pan, and C. K. Ong, "XPS studies of room temperature magnetic Co-doped SnO_2 deposited on Si," Mater. Sci. Eng., B **128**(1-3), 34–36 (2006).
29. S. K. Gullapalli, R. S. Vemuri, and C. V. Ramana, "Structural transformation induced changes in the optical properties of nanocrystalline tungsten oxide thin films," Appl. Phys. Lett. **96**(17), 171903 (2010).
30. X. Zhao, Y. Zhi, W. Cui, D. Guo, Z. Wu, P. Li, L. Li, and W. Tang, "Characterization of hexagonal ε-Ga1.8Sn0.2O_3 thin films for solar-blind ultraviolet applications," Opt. Mater. **62**, 651–654 (2016).
31. D. Guo, Z. Wu, Y. An, X. Guo, X. Chu, C. Sun, L. Li, P. Li, and W. Tang, "Oxygen vacancy tuned Ohmic-Schottky conversion for enhanced performance in β Ga_2O_3 solar-blind ultraviolet photodetectors," Appl. Phys. Lett. **105**(2), 023507 (2014).
32. H. Mosbacker, Y. Strzhemechny, B. White, P. Smith, D. Look, D. Reynolds, C. Litton, and L. Brillson, "Role of near-surface states in ohmic-Schottky conversion of Au contacts to ZnO," Appl. Phys. Lett. **87**(1), 012102 (2005).
33. S. Cui, Z. Mei, Y. Zhang, H. Liang, and X. Du, "Room-temperature fabricated amorphous Ga_2O_3 high-response-speed solar-blind photodetector on rigid and flexible substrates," Adv. Opt. Mater. **5**(19), 1700454 (2017).
34. R. R. Mehta and B. S. Sharma, "Photoconductive gain greater than unity in CdSe films with Schottky barriers at the contacts," J. Appl. Phys. **44**(1), 325–328 (1973).
35. D. Guo, Z. Wu, P. Li, Y. An, H. Liu, and X. Guo, "Fabrication of β-Ga_2O_3 thin films and solar-blind photodetectors by laser MBE technology," Opt. Mater. Express **4**(5), 1067–1076 (2014).
36. N. Liu, G. Fang, W. Zeng, H. Zhou, H. Long, X. Zou, and Y. Liu, "High performance ZnO nanorod strain driving transistor based complementary metal-oxide-semiconductor logic gates," Appl. Phys. Lett. **97**(24), 243504 (2010).
37. P. Mukhopadhyay and W. V. Schoenfeld, "Tin gallium oxide solar-blind photodetectors on sapphire grown by molecular beam epitaxy," Appl. Opt. **58**(13), D22–D27 (2019).
38. Q. Feng, X. Li, G. Han, L. Huang, and Y. Hao, "$(AlGa)_2O_3$ solar-blind photodetectors on sapphire with wider bandgap and improved responsivity," Opt. Mater. Express **7**(4), 1240 (2017).
39. J. A. Garrido, E. Monroy, I. Izpura, and E. Muñoz, "Photoconductive gain modelling of GaN photodetectors," Semicond. Sci. Technol. **13**(6), 563–568 (1998).